Particle and Cell Cluster Separation Based on Inertial Effects in Rectangular Serpentine Channels

Michal Mulík[a] and Ivan Cimrák[b]

*Cell-in-fluid Biomedical Modelling & Computations Group, Faculty of Management Science and Informatics,
University of Žilina, Slovakia*

Keywords: Microfluidics, Inertial Flow, Clusters, PyOIF, ESPResSo, Separation.

Abstract: It is well-established that the inertial effect in microfluidics has a significant impact on particle and cell cluster separation. The outcomes are particularly dependent on the channel geometry and the particle and cell suspensions introduced into the channel. In this study, we investigate various combinations related to the size of a curved channel, fluid velocity, and the size and elasticity of clusters. We quantitatively and qualitatively evaluate the behavior of the examined clusters with respect to separation potential. Computational results suggest specific combinations of flow parameters leading to efficient particle and cell cluster separation.

1 INTRODUCTION

Under specific microflow conditions, fluid inertia dominates over viscous forces, allowing precise control and manipulation of suspended particles (Hood et al., 2015). This has led to the development of techniques to sort and separate particles based on size, shape and deformability (Xu et al., 2021; Nivedita et al., 2017; Liu et al., 2019; Warkiani et al., 2014). Meandering channels induce complex flow patterns and particle behavior due to inertial effects of (Xiang and Ni, 2022). Experimental studies, such as (Tripathi et al., 2016) generating four Dean vortices with two bends and (Zhang et al., 2014) focusing on high-throughput plasma extraction using a secondary flow-assisted inertial microfluidic device, further investigate these phenomena.

The inertial migration of particles was further explored in the work (Bugáňová and Cimrák, 2023), which focused on solid particles and their separation in curved channels of rectangular shape. It was observed that as the particles increase in size, they tend to concentrate and stabilize more in the center of the channel. This leaves a significant space for smaller particles, which concentrate along the edges of the channel, facilitating successful separation. The results demonstrate that not only are smaller cells capable of separating from larger ones, but in some cases,

[a] https://orcid.org/0000-0001-5592-4524
[b] https://orcid.org/0000-0002-0389-7891

they even leave the center of the channel completely empty for a third type of even larger cells. This phenomenon provides an intriguing possibility for triple separation.

Over time, microfluidics has undergone significant breakthroughs and clarifications, allowing for a deeper exploration of phenomena and the continued pursuit of answers to various questions. One such avenue includes the potential opportunity to leverage inertial effects in bio-medicine or medicine in general. In living organisms, such as the human body, inertial flows are encountered, for instance, at vascular bifurcations. The fact that cells divide and travel into different branches provides us with a suitable opportunity to investigate where they are most likely to go. This could enable the capture of rare cells from blood (Tanaka et al., 2012). A similar concept is mentioned in the article (Gossett et al., 2012), where, in the discussion of cell deformation, they were able to separate diseased red blood cells from healthy ones or search for sepsis markers.

In the article (Bugáňová and Cimrák, 2023), detailed information about inertial microfluidics, computational models, and curved microchannels is provided. The study utilized the Lattice-Boltzmann method, a technique also employed in our model. The alignment of cells is correlated with the Reynolds number, directly linked to the fluid velocity. In the model, as the fluid velocity increases, the Reynolds number becomes larger, leading to a more precise stabilization of cells at a specific level within the chan-

553

nel. However, in the mentioned article, the discussion remained focused on the level of small and solid particles that did not have the opportunity to deform. Our work investigates larger objects, which are understandably more prone to deformation. Therefore, we have included this property in our examination.

Contents of this Work

In this study, we employed two geometries of sizes $160 \times 80 \mu m$ and $200 \times 64 \mu m$. For the first time in the model, we introduced rounded edges to better mimic reality, as blood vessels in the body exhibit curvature. We opted for larger geometries compared to those in the article (Bugáňová and Cimrák, 2023) since the cells themselves and the subsequent cell clusters were about two times larger. Consequently, we needed to create a space where cell clusters would have greater freedom in the flow.

In Section 2, we briefly explain inertial forces in microflows. In Section 3, we will explore the fundamental types of channels commonly used in inertial microfluidics worldwide and take a closer look at the model we selected. Specifically, we will focus on two channel sizes. Subsequently, we present the cell and cell cluster model, where we utilized three sizes for each type. Finally, we use two different values of cell elasticity based on the well-known observation that some cells exhibit greater deformability compared to others when exposed to flow in S channels. In the concluding Sections 4.1 and 4.2, we comprehensively summarize the qualitative and quantitative results obtained from our work through simulations. We expect to gain valuable insights into the spatial distribution of the cells over time in relation to the inertial flows, namely Dean flows, induced by the secondary flow.

2 BASIC OVERVIEW OF INERTIAL FOCUSING

The concentration of particles approximately 60% away from the tube centerline in straight channels results from a dynamic equilibrium between inertial shear gradient lift forces, directing the particles towards the wall, and wall repulsion forces generated by elevated pressure between the particles and the channel wall (Matas et al., 2009). Modifying the channel cross-section or introducing curvature through serpentine or spiral geometries alters the distribution and positions of lateral equilibrium, potentially expediting the lateral focusing of particles (Martel and Toner, 2014).

The forces governing this behavior encompass three main components: the wall interaction lift forces, the shear gradient lift forces, and the secondary-flow induced Dean drag forces. All three mentioned mechanisms constitute a complex system where three different principles interact, all dependent on the particle size, channel characteristics, fluid velocity, and the elasticity of particles or cells. Computational modeling can analyze the impact under specific parameters and evaluate the sorting potential of various suspensions.

3 MODEL AND COMPUTATIONAL SETUP

3.1 Numerical Model

We employed a well-established computational model capable of simulating fluid with immersed objects. In this model, the fluid is modelled by the lattice-Boltzmann (LB) method (Arnold et al., 2013). The cell membrane is represented by a network of triangles, and their interaction is determined by elastic coefficients, allowing us to control the magnitude of deformation forces. In our case, we additionally reinforced the cell interiors with edges forming tetrahedral mesh to address the high fluid velocity, which, in a way, limits the deformation of cell clusters. More detailed information on this can be found in the articles (Jančigová et al., 2020; Jancigova and Tothova, 2014; Bachratý et al., 2018). The mentioned model underwent verification and validation for its application, as detailed in (Jančigová et al., 2020; Jančigová, 2020; Tothova et al., 2015).

3.2 Channel Geometry

In (Bugáňová and Cimrák, 2023), the channel geometry with sharp edges was used. In this work, we extended the model with rounded edges, leading to a smoother flow of the fluid as shown in Figure 1. Due to the periodicity of the channel, we will model only two S-sections with periodical boundaries on the inflow and outflow to decrease computational complexity.

Due to the significant computational demands, our model includes only a curved section in the shape of an "S", which was periodically repeated several times until the clusters stabilized in the flow. The basic idea depicted in Figure 2 is that particles or clusters, when initially seeded randomly in the channel near the observation line, flow through one S-section towards a

Figure 1: Separation of cells of different sizes based on the use of a periodically repeating curved channel with round edges in the shape of an "S.".

specific re-seeding line and are subsequently longitudinally re-seeded back to the seeding line by altering the X-coordinates while preserving the Y- and Z-coordinates. This approach allowed us to conduct simulations without creating an entire channel consisting of 40 or 80 repeating S-sections. Moreover, the cluster velocity in the fluid is maintained after the transfer.

In addition to the seeding and re-seeding lines, we also consider an observation line in the middle of the channel. If a cluster passes through this line, we record its center coordinates in a file. The outcome for each cluster is then its trajectory in a graph, illustrating where the cluster has stabilized.
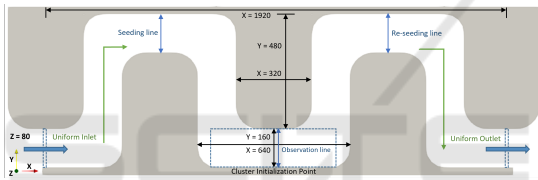

Figure 2: Detailed description of cross-section $160 \times 80 \mu m$. The orientation with respect to the X, Y, and Z axes is described by the three-dimensional axis label in the lower-left corner of the image.

When experimenting with different sizes of the cross section we concluded that cell clusters need sufficient space to rotate freely and for example, cross section 80×40 used in (Bugáňová and Cimrák, 2023) is too narrow for clusters to move out of the center of the cross section. These preliminary tests led to choosing two different channel sizes. The dimensions of both geometries are detailed in Figure 2 for the cross-section $160 \times 80 \mu m$ and Figure 3 for the cross-section $200 \times 64 \mu m$, where all lengths are described in micrometers.
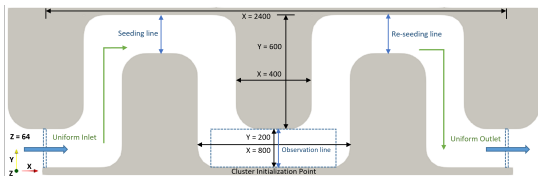

Figure 3: Detailed description of cross-section $200 \times 64 \mu m$. The orientation with respect to the X, Y, and Z axes is described by the three-dimensional axis label in the lower-left corner of the image.

3.3 Fluid Set-up

The imposition of uniform boundary conditions at the inlet and outlet serves to determine the average velocity within the channel, a factor directly proportional to the volumetric flow rate. In the PyOIF framework, achieving this involves implementing a specialized velocity boundary equipped with pre-defined constant values for the velocity field at the boundary points.

Values of the inlet conditions and the corresponding Reynolds numbers are presented in Table 1.

Table 1: Fluid velocity parameters in $160 \times 80 \mu m$ curved channel. Values in the other cross-section are similar.

Reynolds number $[-]$	19.2	37.3	48	64
Average velocity $[\mu m/\mu s]$	0.18	0.35	0.45	0.6

Our focus lies in examining flows within scenarios that hold physical relevance. Specifically, we investigate fluids with a density and viscosity akin to physiological solutions or water, characterized by values of $1000 kg/m^3$ and $10^{-3} Pa.s$, respectively. In the sphere of inertial microfluidics, where the Reynolds number is a pertinent parameter, we adhere to ranges up to 100 (Ying and Lina, 2020). To encompass a diverse set of conditions, we explore four distinct average velocities within the channel, reaching up to $0.6 \mu m/\mu s$, thereby allowing the Reynolds number to vary up to 64.
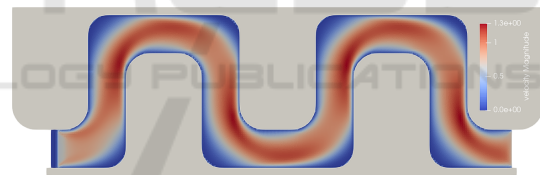

Figure 4: The fluid flowing in the channel at the highest Reynolds number 64. The units of the displayed scale are in $\mu m/\mu s$.

A visual representation of the fluid flowing throughout the simulation can be seen in Figure 4. The more saturated red color, the higher the fluid velocity at that location. Flow direction is from left to right. The areas with deep blue indicate almost zero fluid velocity.

3.4 Cell and Cluster Models

Similar to the membrane model of red blood cells composed of triangular mesh, the cluster model is composed of a tetrahedral mesh. Given the presence of stiffer cancer clusters, we reinforced the cell's interior with additional edges forming complete cover of cell's interior by tetrahedrons to restrict excessive deformation due to the high fluid velocity in the simulation. The edges of tetrahedrons are modelled as

springs with given relaxed length and specific stiffness. To get stiffer cells or clusters, higher values of edge stiffness was used. In Figure 5, the interiors of a single cell and a cluster are depicted, respectively.

As a model for cancer cells, we opted for a spherical shape as it closely approximates the morphology of most real types of cancer cells within the body. The length of tetrahedral edges was primarily determined by the size of the object, as the number of points in the tetrahedral network remained constant.
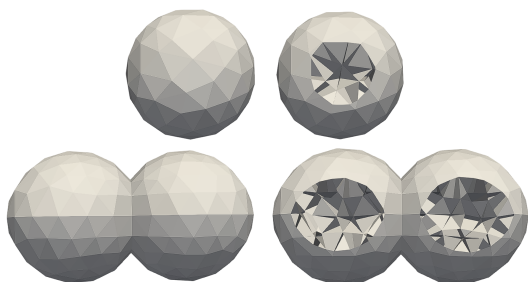

Figure 5: The entire cell (top left), cutaway of the cell (top right), the entire cluster (bottom left) and a cutaway of the cluster (bottom right). The cuts reveal the interiors filled with walls.

Based on the actual sizes of cancer cell clusters, we determined three basic sizes for a cluster with a single cell and three for a cluster with two cells. On closer inspection, in one case, the size of a single cell is even equal to that of two cells placed side by side. A comparison of sizes for clusters containing one or two cells is illustrated in Figure 6.
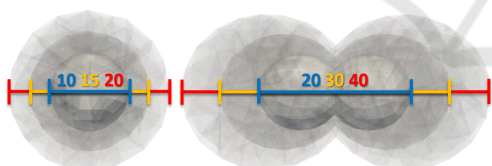

Figure 6: The cluster containing a single cell (left), and the cluster with two cells (right). Sizes are given in micrometers.

The cell adhesion in a cluster can be simulated in two different ways. One way is to use an attractive-repulsive Lennard-Jones or Morse-type interaction, where two separate cells are attracted to each other when they are far apart and repelled when they are too close. This approach ensures that cells can slide past each other, and at high fluid velocities, it may lead to their separation. However, the fluid velocity we use almost always separates these cells, making it an unsuitable method.

Another way for cells to be connected in a cluster is by such a strong bond that cells do not slide over each other and the bond is fixed. To simulate this behavior, we used the second method of connecting cells through a shared membrane. In this case, the entire cluster behaves as one object. As seen in Figure 6 on the right, the cluster contains two connected cells. These methods that help us simulate the cell adhesion in a cluster are described in more detail in the article (Jančigová et al., 2022).

4 COMPUTATIONAL RESULTS

In this section, we will delve into the results of simulations in an S-shaped curved channel. In this case, we utilized a single basic cluster of two cells (hereinafter referred to as the "two-in-line" cluster). However, technically, we will also treat a single cell as a cluster of cells composed of only one cell, which we now refer to as "CTC", an acronym for "circulating tumour cell". For each cluster type, we will distinguish three different sizes concerning the diameter. For the two-in-line cluster we used diameters of 20, 30, and 40 μm, meaning that one cell in the two-in-line cluster had a diameter of 10, 15, and 20 μm. For the single-cell cluster, we aimed to approach its largest size to the smallest two-in-line cluster, so we chose the same diameters of 10, 15, and 20 μm. The sizes of clusters were chosen based on the article (Anderson et al., 2017).

In addition to the cluster type and size, we incorporated the elasticity of the cell. Clusters were divided into more and less elastic ones under the names "solid" and "elastic". Solid clusters represented the stiffest cells that had almost no possibility of deformation during flow in the channels, while elastic ones had the ability to deform. It should be noted that both types of clusters had an internal fill, so we will talk about one important and only used elastic parameter called k_s, which represents the edge stiffness. The difference between elastic cluster with $k_s = 0.5$ and solid cluster with $k_s = 1.0$ can be seen in Figure 7. Top row depicts clusters close to the channel center with low shear rates. This implies minimal deformation of the clusters. The second row depicts clusters at positions near the wall with high shear rates, leading to significant deformation of more elastic cluster while the solid one remains fairly rigid. The simulations in Figure 7 were conducted at $Re = 64$.

As mentioned before, we conducted simulations with four fluid velocities corresponding to four values of Reynolds number, as indicated in Table 1. For completeness, it should be noted that we used two different channel sizes with cross-sections of $160 \times 80 \mu m$ and $200 \times 64 \mu m$. Further details about individual channel geometries are already described in Section 3.2.
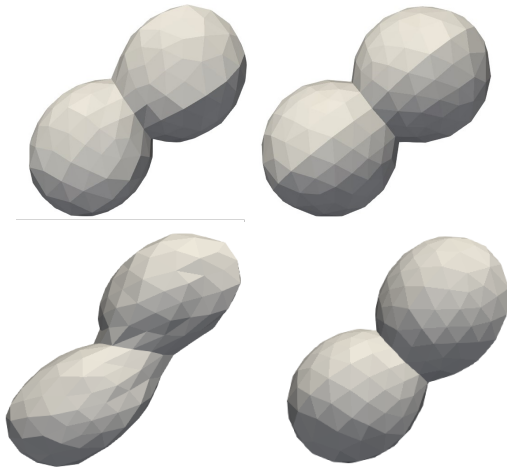
Figure 7: The deformation of a two-in-line cluster with $k_s = 0.5$ (left column) and $k_s = 1.0$ (right column). Deformation at low shear rates depicted in top row and at high shear rates in bottom row.

The initial seeding line for generating cluster positions is delineated in Figures 2 and 3. Distinct random positions for clusters were generated for each geometry. Additionally, the initial rotation of clusters was randomized for each geometry, given the absence of a clear explanation regarding whether the initial rotation significantly influences simulation outcomes. As these are simple clusters composed of one or two cells, we did not attribute significant emphasis to this aspect.

All numerical results were subsequently represented by graphs, facilitating comparisons. In the following Subsections 4.1 and 4.2, we will present the most useful comparisons.

4.1 Quantitative Analysis of Flow Patterns

From a quantitative perspective, we focused on analyzing data obtained from simulations, categorizing it into five parts for better clarity: channel geometry, fluid velocity, cluster type, cluster size, and cluster elasticity, in that order. All results were primarily compared in terms of the separation of different clusters, where the main role was played by inertial flow, specifically the Dean effect.

For a general overview, each simulation included 28 clusters of cells. The simulation ran until each cluster crossed the observation line 40 times. However, it should be noted that especially at the highest fluid velocity $Re = 64$ and channel size of $160 \times 80 \mu m$ with CTCs, we concluded that they did not have enough time to stabilize within 40 passes. Therefore, we increased the number of passes to 80 for them to

stabilize more effectively within the flow. For comparison, you can refer to Figure 8, where a significant difference between 40 and 80 passes is evident. For all subsequent comparisons in graph form, results from 80 passes were used.

For quantitative analysis, Figure 9 serves us the most, where it is clearly visible that in some cases, clusters can linger near the channel walls, creating space in the middle of the channel for other clusters that can be separated from the other lateral clusters.

4.1.1 Analysis of CTCs

At first glance, CTCs in graphs (C), (D), (G), and (H) seem to linger the most on the sides of the channel. The only differences are the solid and elastic CTCs in graphs (C) and (D) for the geometry of $160 \times 80 \mu m$, fluid velocity $Re = 64$, and a diameter of $20 \mu m$, which linger more in the middle of the channel. Based on the obtained information, we can infer that they can be separated from the smallest CTCs with a diameter of $10 \mu m$. It should be mentioned that in the (H) graph, the largest CTCs at the slowest speed are scattered across the entire width. This result is due to the small number of passes, as the cells have not yet had time to settle. For a better understanding, we can observe the changes in the ongoing settling in Figure 10.

4.1.2 Analysis of Two-in-Line Clusters

In the case of two-in-line clusters, the behavior in the flow is not that straightforward. The trend for the largest clusters remains consistent with single-cell clusters, settling in the center of the channel. The only instances where they concentrate at the channel edges occur at the highest velocity, $Re = 64$, and a geometry of $160 \times 80 \mu m$, as seen in graphs (A) and (B) in the last columns marked in red. Conversely, the smallest two-in-line clusters marked in blue tended to settle regularly at the channel edges. Exceptions are specific cases, as observed in graphs (B) and (C) at $Re = 48$ and graph (F) at $Re = 19.2$.

Medium-sized two-in-line clusters marked in yellow generally behaved similarly to two-in-line clusters, except for isolated cases observed in graphs (A) and (E), where the settling level coincided with the smallest two-in-line clusters. From the analysis, it can be inferred that there is a possibility of separating two-in-line clusters from other two-in-line clusters based on their sizes, as seen in the mentioned graph (E) at all fluid velocities or at specific fluid velocities in graphs (A), (B), or (F).

An interesting aspect is that for two-in-line clusters, elasticity plays a role for the first time, as we could potentially separate clusters with diameters 20
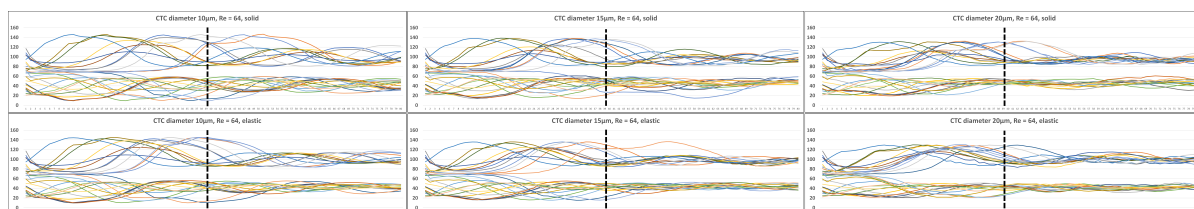
Figure 8: Examples of a cluster formed by CTCs with a diameter of 10, 15 and $20\mu m$, solid and elastic type, at a cross-section of $160 \times 80\mu m$. The Y-axis represents the channel width, and the X-axis represents the number of passes. The dashed line indicates the state after 40 passes through the channel.
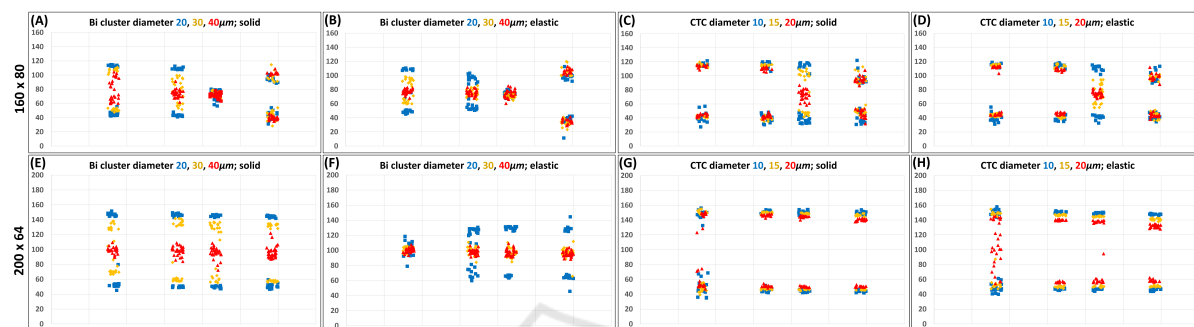

Figure 9: Complete set of 96 simulations, where each graph contains exactly 12 of them. Each graph has 4 columns for 4 values of Reynolds number mentioned in Table 1 from the smallest to the largest from left to right. Each column has results from three simulations, differing in the cluster size. Regarding the legends, blue squares represent the smallest clusters, yellow diamonds represent medium-sized clusters, and red triangles represent the largest clusters. In general, these are analogously transformed graphs from 8 into a concise form for better visualization, where data were taken only from the last passage of all cells in the simulation. All graphs indicate the locations where cell clusters stabilized. The first row of graphs A-D denotes the last passage of cells from channels with cross-section $160 \times 80\mu m$, and the second row E-H with cross-section $200 \times 64\mu m$. Graphs (A), (B), (E), and (F) represent the stabilization of two-in-line clusters, and graphs (C), (D), (G), and (H) of CTCs. Regarding the elasticity of clusters, graphs (A), (C), (E), (G) are solid, and (B), (D), (F), and (H) are elastic.
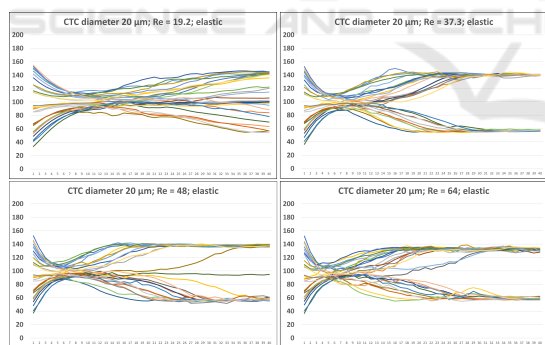

Figure 10: The graphs represent the settling of elastic CTCs over 40 passes, ranging from the slowest fluid speed, where $Re = 19.2$, to the fastest, where $Re = 64$. In this case, a cross-section of $200 \times 64\mu m$ was used, and the cells were elastic.

and $30\mu m$, that have different elasticity. This phenomenon can be observed, for example, by comparing graphs (E) and (F) at the lowest velocity $Re = 19.2$ in case of the smallest clusters, and at all velocities in case of medium-sized clusters, where solid clusters concentrate on the sides of the channel, and elastic clusters in its center.

4.1.3 Comparison Between CTC and Two-in-Line Cluster

When comparing the same geometries but different clusters, namely CTC and two-in-line clusters, we come to the conclusion that separation is also possible under certain conditions. Considering the first row of graphs with the $160 \times 80\mu m$ geometry, the smallest two-in-line clusters with a diameter of $20\mu m$ in graphs (A) and (B) could be separated from CTC in graphs (C) and (D) with a diameter of $10\mu m$, for example, at a fluid velocity of $Re = 48$. This is because CTC would again stabilize at the sides of the channel, while two-in-line clusters would stabilize in the center.

The same case applies to medium-sized and the largest two-in-line clusters with diameters of 30 and $40\mu m$. However, the largest two-in-line clusters at a fluid velocity of $Re = 37.3$ could be separated from any size of CTC. The same applies to $Re = 19.2$ and elastic two-in-line clusters. However, the geometry $200 \times 64\mu m$, which provides more space for cell stabilization at the sides of the channel due to its wider width, offers a more obvious separation possibility.

For the smallest elastic two-in-line cluster in graph (F), there is an opportunity for separation at the slow-

est fluid velocity of $Re = 19.2$ from any size of CTC in graphs (G) and (H). In this case, the separation possibility for elastic CTC would depend on the number of passes. The same applies when considering medium-sized and elastic two-in-line clusters in graph (F), where the separation is possible regardless of the fluid velocity Re chosen. However, the largest two-in-line clusters could probably be separated most effectively from any size of CTC, as it is independent of both elasticity and fluid velocity.

4.2 Qualitative Analysis of Flow Patterns

From a qualitative perspective, we observed the flow of CTC and two-in-line clusters in the $160 \times 80\mu m$ channel. The movement of a single solid two-in-line cluster can be seen at the highest velocity in Figure 11, depicting the cluster's movement in three consecutive S-sections. The cluster's motion was recorded after approximately 20 passes, indicating a steady flow.

At first glance, collisions with the wall can be observed at each upper right turn. Two-in-line clusters, in general, do not have a reason to rotate around their center. Nevertheless, during gentle shear flow generated by collisions and movement along the wall, the cluster tends to rotate around its own center a few times in succession. This rotation involves a change in the order of cells, with the most pronounced rotations occurring during the first two upper turns, as the cluster is aligned longitudinally along the X-axis. In the third turn, where the cluster is aligned widthwise, this rotation type does not occur. In this case, the cluster appears to rotate like a wheel.

It is important to note that collisions of CTC and clusters with walls are not entirely safe from a human health perspective. Further information on the interactions of clusters with walls can be found in the article (Jančigová et al., 2022).

Figure 11: Three S-shaped channel passes of the largest solid two-in-line cluster in the geometry of $160 \times 80\mu m$ at the highest velocity of $Re = 64$. One cell out of two is marked in red to better observe the movement, especially the rotation of each cell in the cluster.

5 CONCLUSION

The basis of the work was derived from the principles of inertial flows, namely Dean flows. Thanks to them, we could observe how clusters, after several passes through the channel, slowly stabilized either in the center or at the edges of the channel. This phenomenon allowed us to study the separation of cell clusters, which depended on their properties or the properties of the surrounding environment in the model in which we released them.

Initially, we worked on a model of a microfluidic channel in an S shape, which had rounded edges for simpler fluid flow. As a next step, we created new channel geometry sizes with dimensions of $160 \times 80\mu m$ and $200 \times 64\mu m$ to provide more space for the stabilization of cell clusters.

We focused mainly on studying a simple cluster formed from a single cell, also known as CTC, and a two-in-line cluster formed from two cells. Fluid was released at four different velocities expressed by the Reynolds number $Re = 19.2, 37.3, 48,$ and 64, in which we released clusters with three different cell diameters, $10, 15,$ and $20\mu m$. These clusters also had two different elasticities, so some were solid, where $k_s = 1.0$, and others were elastic, for which $k_s = 0.5$, meaning they had more opportunity to deform during the simulation than solid ones.

As for the computational complexity of each simulation, each one ran for 3 to 7 days until each cluster in the simulation had a certain number of passes. Mostly, it was 40 passes. In a specific case where it took longer for the clusters to stabilize, we increased the number of passes to 80.

The obtained numerical data of cluster positions were analyzed from each simulation using appropriate graphs. We summarized and combined all the graphs, where it was very well visible which clusters stabilized at the edges of the channel and which, on the contrary, more in its central part with respect to the channel height, i.e., the Y-axis. For some combinations of sizes and elasticity of CTC and clusters, we found that separation would be highly probable.

REFERENCES

Anderson, K. J., de Guillebon, A., Hughes, A. D., Wang, W., and King, M. R. (2017). Effect of circulating tumor cell aggregate configuration on hemodynamic transport and wall contact. *Mathematical biosciences*, 294:181–194.

Arnold, A., Lenz, O., Kesselheim, S., Weeber, R., Fahrenberger, F., Roehm, D., Košovan, P., and Holm, C. (2013). ESPResSo 3.1: Molecular dynamics software for coarse-grained models. In *Meshfree Methods for Partial Differential Equations VI*, Lecture notes in computational science and engineering, pages 1–23. Springer Berlin Heidelberg, Berlin, Heidelberg.

Bachratý, H., Bachratá, K., Chovanec, M., Kajánek, F., Smiešková, M., and Slavík, M. (2018). Simulation of blood flow in microfluidic devices for analysing of video from real experiments. In *Bioinformatics and Biomedical Engineering*, Lecture notes in computer science, pages 279–289. Springer International Publishing, Cham.

Bugáňová, A. and Cimrák, I. (2023). Computational study of particle separation based on inertial effects in rectangular serpentine channels with different aspect ratios. In *Proceedings of the 16th International Joint Conference on Biomedical Engineering Systems and Technologies (BIOSTEC 2023) - Volume 3: BIOINFORMATICS*, pages 284–291. INSTICC, SciTePress.

Gossett, D. R., Tse, H. T. K., Lee, S. A., Ying, Y., Lindgren, A. G., Yang, O. O., Rao, J., Clark, A. T., and Di Carlo, D. (2012). Hydrodynamic stretching of single cells for large population mechanical phenotyping. *Proc. Natl. Acad. Sci. U. S. A.*, 109(20):7630–7635.

Hood, K., Lee, S., and Roper, M. (2015). Inertial migration of a rigid sphere in three-dimensional poiseuille flow. *J. Fluid Mech.*, 765:452–479.

Jančigová, I. (2020). Computational modeling of blood flow with rare cell in a microbifurcation. In *Lecture Notes in Computational Vision and Biomechanics*, Lecture notes in computational vision and biomechanics, pages 518–525. Springer International Publishing, Cham.

Jančigová, I., Kovalčíková, K., Bohiniková, A., and Cimrák, I. (2020). Spring-network model of red blood cell: From membrane mechanics to validation. *Int. J. Numer. Methods Fluids*, 92(10):1368–1393.

Jancigova, I. and Tothova, R. (2014). Scalability of forces in mesh-based models of elastic objects. In *2014 ELEKTRO*. IEEE.

Jančigová, I., Kovalčíková, K., Weeber, R., and Cimrák, I. (2020). Pyoif: Computational tool for modelling of multi-cell flows in complex geometries. *PLoS Computational Biology*, 16:e1008249.

Jančigová, I., Mulík, M., and Cimrák, I. (2022). Contact area of cell cluster in a simple bifurcation. In *2022 ELEKTRO (ELEKTRO)*, pages 1–5.

Liu, N., Petchakup, C., Tay, H. M., Li, K. H. H., and Hou, H. W. (2019). Spiral inertial microfluidics for cell separation and biomedical applications. *Applications of Microfluidic Systems in Biology and Medicine*, pages 99–150.

Martel, J. M. and Toner, M. (2014). Inertial focusing in microfluidics. *Annu. Rev. Biomed. Eng.*, 16(1):371–396.

Matas, J.-P., Morris, J. F., and Guazzelli, É. (2009). Lateral force on a rigid sphere in large-inertia laminar pipe flow. *J. Fluid Mech.*, 621:59–67.

Nivedita, N., Ligrani, P., and Papautsky, I. (2017). Dean flow dynamics in low-aspect ratio spiral microchannels. *Scientific Reports*, 7(1):44072.

Tanaka, T., Ishikawa, T., Numayama-Tsuruta, K., Imai, Y., Ueno, H., Matsuki, N., and Yamaguchi, T. (2012). Separation of cancer cells from a red blood cell suspension using inertial force. *Lab Chip*, 12(21):4336–4343.

Tothova, R., Jancigova, I., and Busik, M. (2015). Calibration of elastic coefficients for spring-network model of red blood cell. In *2015 International Conference on Information and Digital Technologies*. IEEE.

Tripathi, S., Kumar, A., Bala Varun Kumar, Y., and Agrawal, A. (2016). Three-dimensional hydrodynamic flow focusing of dye, particles and cells in a microfluidic device by employing two bends of opposite curvature. *Microfluidics and Nanofluidics*, 20:1–14.

Warkiani, M. E., Guan, G., Luan, K. B., Lee, W. C., Bhagat, A. A. S., Chaudhuri, P. K., Tan, D. S.-W., Lim, W. T., Lee, S. C., Chen, P. C., et al. (2014). Slanted spiral microfluidics for the ultra-fast, label-free isolation of circulating tumor cells. *Lab on a Chip*, 14(1):128–137.

Xiang, N. and Ni, Z. (2022). Inertial microfluidics: current status, challenges, and future opportunities. *Lab on a Chip*, 22(24):4792–4804.

Xu, X., Huang, X., Sun, J., Wang, R., Yao, J., Han, W., Wei, M., Chen, J., Guo, J., Sun, L., et al. (2021). Recent progress of inertial microfluidic-based cell separation. *Analyst*, 146(23):7070–7086.

Ying, Y. and Lina, Y. (2020). Inertial focusing and separation of particles in similar curved channels. *Scientific reports, natureresearch*, 391:123570.

Zhang, J., Yan, S., Li, W., Alici, G., and Nguyen, N.-T. (2014). High throughput extraction of plasma using a secondary flow-aided inertial microfluidic device. *RSC Adv.*, 4:33149–33159.